New constraints on the origin of the Hawaiian swell from wavelet analysis of the geoid to topography ratio

Cécilia Cadio [a,b,*], Maxim D. Ballmer [c], Isabelle Panet [b,d], Michel Diament [b], Neil Ribe [e]

[a] Department of Geology and Geophysics, Yale University, New Haven, CT 06511, USA
[b] Université Paris Diderot, Sorbonne Paris Cité, Institut de Physique du Globe de Paris, CNRS, Paris, France
[c] Department of Geology and Geophysics, School of Ocean and Earth Sciences and Technology, University of Hawaii at Manoa, Honolulu, HI 96822, USA
[d] Institut National de l'Information Géographique et Forestière, Laboratoire de Recherche en Géodésie, GRGS, Paris, France
[e] Laboratoire FAST, UPMC/Université Paris-Sud/CNRS, Orsay, France

ARTICLE INFO

ABSTRACT

Analyzing the formation mechanism of hotspot swells enhances our understanding of intraplate volcanism and the underlying geodynamical processes. The two main hypotheses for the origin of the archetypal Hawaiian swell are thermal lithospheric thinning, and dynamic support by an ascending plume. Any successful model would have to be able to simultaneously explain the swell topography and the corresponding geoid anomaly. In simple models of isostatic compensation, the geoid-to-topography ratio (GTR) is linearly related to the depth of the compensating mass; therefore it is often considered a fundamental parameter to assess swell support mechanisms. Previous estimates for the geoid-to-topography ratio (GTR) of the Hawaiian swell however are biased towards low values by incomplete removal of the effects of volcanic loading and lithospheric flexure. In order to resolve these issues, we here apply a continuous wavelet transform, which allows resolution of lateral variations of the GTR at various spatial scales. In a series of synthetic tests, the robustness of this approach and its power to identify the origin of hotspot swells are established. With 8 m/km on the youngest part of the chain, the recovered GTR agrees well with the predictions for dynamic support, therefore ruling out thermal rejuvenation as an important mechanism. We also find that the depth of the compensating mass decays by 20 km over a distance of 500 km from Hawaii to Kauai, and identify sublithospheric erosion by small-scale convection in the ponded plume material as a viable mechanism to support this decay.

Published by Elsevier B.V.

1. Introduction

Along with volcanic islands and seamount chains, regional highs in seafloor topography, or "swells", are the main surface expressions of hotspot activity (Crough, 1983). Analyzing the formation of hotspot swells is critical for understanding the origin of intraplate volcanism, the underlying mantle dynamics in the asthenosphere and at the base of the lithosphere, as well as the rheology of the upper mantle. For example, such an analysis may enable to discriminate between plume and non-plume origins of hotspots. Of all these remarkable topographic features, the Hawaiian swell, first described by Dietz and Menard (1953), is the best-studied example (Fig. 1). Emplaced over a span of only a few million years (Crough, 1978), it manifests itself as a broad topographic rise some 1200 km wide and 3000 km long,

surrounding the youngest part of the chain. The height of the swell (excluding the islands) culminates at almost 1400 m close to the active hotspot center (Parsons and Sclater, 1977; Crosby and McKenzie, 2009) and slowly decays along the island chain to the northwest.

Two models have classically been considered to explain Hawaiian swell formation: "thermal rejuvenation" and "dynamic support". According to the thermal rejuvenation model, the hotspot heats the lower part of the lithosphere, effectively replacing it by less dense asthenosphere that pushes up the plate (Crough, 1978; Detrick and Crough, 1978; McNutt, 1984). In the dynamic support model, the swell is instead supported by the mantle plume itself, which exerts normal stresses on the base of the lithosphere by being deflected into a buoyant "pancake" of hot plume residue (Parsons and Daly, 1983; Olson, 1990; Ribe and Christensen, 1994, 1999; Cserepes et al., 2000).

Any formation model for the swell must simultaneously explain its two main characteristics: the topography and the corresponding geoid anomaly. If isostatic equilibrium is attained, the mass excess related to seafloor topography is compensated by

* Corresponding author at: Yale University, Department of Geology and Geophysics, New Haven, CT 06511, USA. Tel.: +1 203 432 1094.
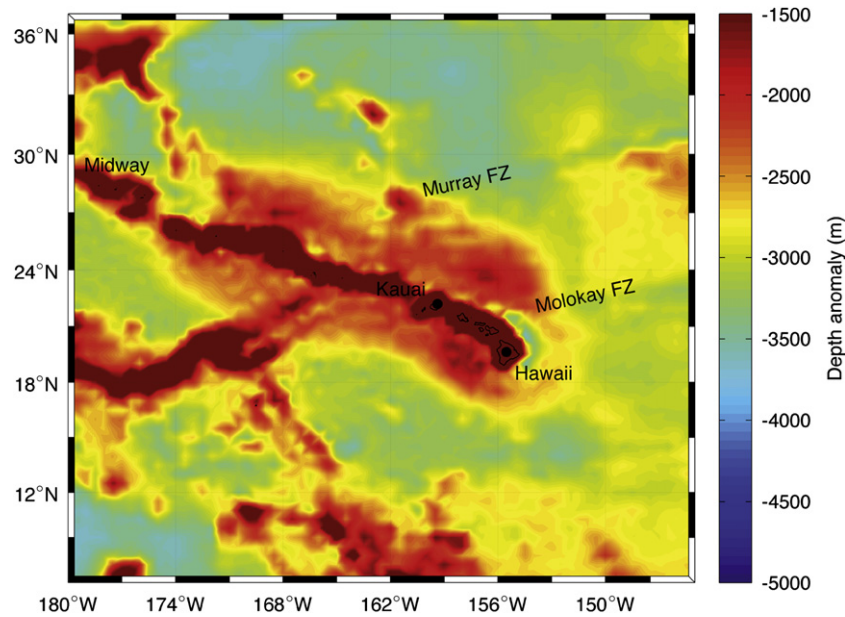E-mail address: cecilia.cadio@yale.edu (C. Cadio).

Fig. 1. Representation of the bathymetric grid GEBCO that shows the Hawaiian Islands and the surrounding swell. Over an area of ~3000 km along the Hawaiian chain and ~1200 km across, the seafloor is anomalously shallow. The relative height of this swell peaks at ~1400 m near the intersection of Molokai Fracture Zone and the island chain.

an equal mass deficit at depth, thus resulting in a positive geoid anomaly, of which the amplitude depends on the depth of the compensating density anomaly (e.g. Haxby and Turcotte, 1978). For example, a sinusoidal density anomaly $\Delta\rho$ at a given depth D and wavenumber k compensates an associated topography of amplitude h and thus perturbs the geoid N (Crough, 1978):

$$\Delta N = \frac{2\pi G\rho h}{gk}\left[1-\exp(-kD)\right]\cos(kx),\qquad(1)$$

with G as the gravitational constant, and g as the mean surface gravity. At the spatial scales of the swell (i.e. for k tending to 0), the ratio between the geoid and topography is linearly related to the apparent compensation depth (i.e. the average depth of compensating density anomalies) D:

$$\frac{\Delta N}{h} = \frac{2\pi G\rho D}{g}.\qquad(2)$$

For reasonable values of $\Delta\rho$, a simple rule of thumb is obtained: $(\Delta N/h)\,(m/km) = 0.1 \times D\,(km)$. This ratio is therefore often considered as a fundamental parameter to assess swell support mechanisms. A low ratio (> 2 m/km) indicates that the topography is supported by thickened crust. In contrast, an intermediate ratio (2–6 m/km) signifies deeper compensation in the lithospheric mantle such as by thermal rejuvenation (Crough, 1978). Finally, a high ratio (> 6 m/km) indicates compensation within the asthenosphere such as by dynamic uplift (Parsons and Daly, 1983). Along these lines, the joint analysis of the geoid and topography anomalies, by calculating the geoid-to-topography ratio (GTR), potentially allows to discriminate between the different physical mechanisms that generate the Hawaiian swell, and indirectly to assess the origin of the associated intraplate volcanism.

The thermal rejuvenation and dynamic support models differ by the depth of the low-density compensating material, which is entirely located either above the base of "normal" lithosphere of that age in the first case or below in the second case. These two end-member models are reasonably successful to qualitatively predict swell morphology but both remain incomplete. The thermal rejuvenation model has difficulties to explain the steep

slope at the leading edge of the swell (i.e., its rapid uplift < 5 Ma; Crough, 1978), and to reconcile the apparent lack of a heat flow anomaly (Von Herzen et al., 1989; Harris et al., 2000). The dynamic support model can neither account for the low observed GTR values on the Hawaiian swell between 3.5 and 6 m/km (Crough, 1978; McNutt and Shure, 1986; Cazenave et al., 1988; Sandwell and Renkin, 1988; Sandwell and MacKenzie, 1989; Marks and Sandwell, 1991), nor for seismic constraints that indicate 10–50 km lithospheric thinning such as seen in receiver functions (Li et al., 2004), and underside reflections (Schmerr, 2012).

In order to resolve some of these discrepancies, a new hybrid model has recently been outlined for the origin of the Hawaiian swell (Ribe, 2004). Vigorous small-scale convection (SSC) may develop within the plume pancake (Moore et al., 1998, 1999), and gradually erode the base of the lithosphere (Ballmer et al., 2011). Accordingly, the swell as a whole would be mainly supported dynamically with additional and increasing support by lithospheric thinning towards the northwest. This gradual decrease of the compensation depth along the swell should produce lateral variations of the GTR. Such a model may explain both the rapid uplift of the swell and the amount of lithospheric thinning inferred from seismology. The rates of thermal erosion of the lithosphere along the chain are indeed compatible with the typical timescales of SSC (Yuen and Fleitout, 1985; Sleep, 1994; van Hunen et al., 2003). Moreover, Ballmer et al. (2011) recently showed that the interaction of such SSC with a plume can also give an explanation for geochemical asymmetry in Hawaiian volcanism (Abouchami et al., 2005), and the occurrence of secondary volcanism (Garcia et al., 2010). Testing this hybrid model against the two classical models critically depends on the ability to resolve possible lateral variations of the GTR.

So far, the GTR has usually been estimated from the slope of the regression line of the geoid versus the topography for the entire swell region (cf. Marks and Sandwell (1991) for a detailed review). Bandpass filters have been applied to the data in order to retain wavelengths that are related to the swell structure and compensation mechanism only. The characteristic wavelength range of interest lies between 400 and 4000 km for Hawaii.

While the spatial scales shorter than 400 km result from volcanic loading and the related elastic flexure of the lithosphere, the wavelengths longer than 4000 km are typically associated with density heterogeneities of the deep mantle and cooling of the lithosphere.

The obtained values for the GTR of the Hawaiian swell scatter between 3.5 and 6 m/km (Crough, 1978; McNutt and Shure, 1986; Cazenave et al., 1988; Sandwell and Renkin, 1988; Sandwell and MacKenzie, 1989; Marks and Sandwell, 1991), a range that suggests an intra-lithospheric compensation due to thinning of the lithosphere (Crough, 1978) or a dynamic support but associated with a low-viscosity asthenosphere (Robinson et al., 1987; Robinson and Parsons, 1988; Ceuleneer et al., 1988). However, these figures appear to be inconsistent with predictions based on geodynamic models with temperature-dependent viscosity, which yield higher values (7–8 m/km; Ribe and Christensen, 1999). Two major shortcomings are associated with any of the previous approaches: first, the common assumption of a single compensation depth for the entire swell does not allow detection of any potential variation in compensation depth along the chain, as e.g. suggested by the hybrid model. Second, the applied bandpass filters cannot completely remove unwanted signals such as those related to volcanic surface loading, an error that has been shown to lead to underestimation of the GTR (Cserepes et al., 2000).

In order to address these shortcomings and to understand Hawaiian swell formation, we apply a more advanced method to a new set of data. We calculate the ratio between the geoid and topography using a spatio-spectral admittance function, which is defined as the ratio of the wavelet cross-spectrum of the geoid and topography to the wavelet power spectrum of the topography (McKenzie and Bowin, 1976; Stark et al., 2003; Daly et al., 2004; Kirby and Swain, 2004; Audet, 2011). The wavelet approach allows precise separation of the different geoid and topography components in the spatial and spectral domains, and thus to study the variations of the GTR at different spatial scales along the Hawaiian island chain. In a first step, we test the robustness of the wavelet method with different synthetic cases, some of which are based on geodynamic models of Hawaiian swell formation. In the second step, we apply this new method to the Hawaiian swell to quantify the amplitude of the GTR and to resolve its spatial variations. Here, we benefit from the high-quality gravity data set from the GRACE mission. Finally, in order to assess the physical mechanisms of Hawaiian swell formation, we compare these results with the synthetic tests from geodynamic models and recent seismic observations.

2. Wavelet admittance and coherence

The spectral properties of the geoid and topography generally vary as a function of position. A straightforward approach to localize a geophysical signal is to analyze the data with a localizing function. Therefore, we apply a continuous wavelet transform (CWT) to both the geoid and topography. The CWT is constructed from a set of analysis coefficients as defined from the correlation between the signal and an analyzing wavelet at a given spatial scale and position. Since the investigated scales and positions vary continuously, such an analysis enables to emphasize the components of the signal and to finely characterize its local features across a range of scales (Holschneider, 1995).

A wavelet is a piecewise continuous function with zero mean and finite energy, well localized both in the spatial and spectral domains. It should be noted however that this localization is bounded by the uncertainty principle, which states that there is a trade-off between spatial and spectral localization. For a given
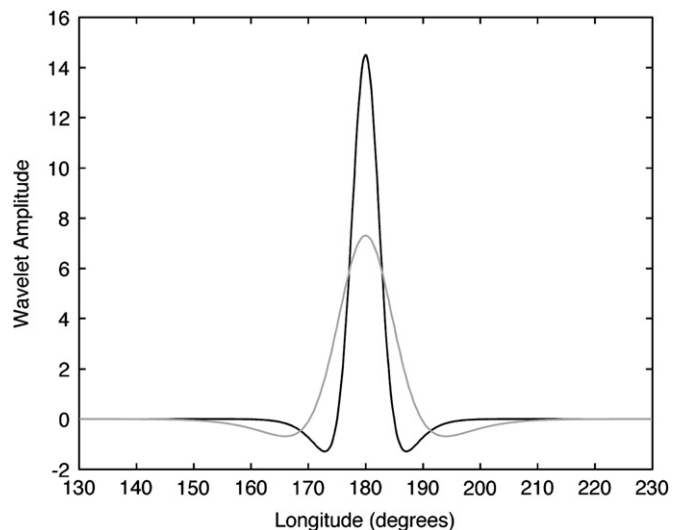

Fig. 2. Cross section of Poisson multipole wavelets of order 3 and scales 1000 (black curve) and 2000 (grey curve) km centered at point (0°N, 180°E).

wavelet family, each function is described with two parameters: the position parameter (e) defines the point around which the wavelet concentrates its energy in the spatial domain (its center), and the scale parameter (a) reflects its spatial extent. Wavelets can be regarded as local bandpass filters, with the center of the bandwidth defined by the scale parameter.

Here we use spherical Poisson multipole wavelets of order 3 that have been described by Holschneider et al. (2003) and Chambodut et al. (2005). Fig. 2 represents a cross-section of these wavelets at two different scales, all located at (0°N, 180°E). Such wavelets are particularly well suited to analyze potential fields. Because they can be expressed as a series of Legendre polynomials, these functions allows us to easily analyze geoid anomalies derived from a global spherical harmonic model. Moreover, these wavelets may be identified with multipoles of order m (or equivalent sources) whose depth is directly related to the scale parameter. Applications of these wavelets can be found in Panet et al. (2006, 2007) and Cadio et al. (2011).

The wavelet admittance Z^ψ corresponds to a local transfer function between the topography h and the geoid N. It illustrates the spatial variations of the GTR at different scales. The admittance is obtained by dividing the wavelet cross-power spectra of the geoid and the topography signals $P^\psi_{N,h}$ by the wavelet auto-power spectra of the topography $P^\psi_{N,h}$ (Stark et al., 2003; Daly et al., 2004; Kirby and Swain, 2004; Audet, 2011). The admittance Z^ψ at the scale a and the point x is given by

$$Z^\psi(a,x) = \frac{P^\psi_{N,h}(a,x)}{P^\psi_{h,h}(a,x)}. \tag{3}$$

The local wavelet cross-power spectra of the geoid and the topography $P^\psi_{N,h}$ are defined as the product of the CWT coefficients of each signal, averaged over a window, of which the width depends on the scale of the analyzing wavelet:

$$P^\psi_{N,h}(a,x) = \int C_N(a,e)C_h(a,e)\Phi_{sa}(x-e)de \tag{4}$$

with $C_N(a,e)$ and $C_h(a,e)$ as the CWT coefficients at the scale a in position e of the geoid and of the topography, respectively. Here, Φ corresponds to the averaging window, centered on position x with a finite width sa. Averaging is applied to reduce the effects of noise (McKenzie and Bowin, 1976). However, it also smooths the spatial variations of the wavelet cross-power spectra and
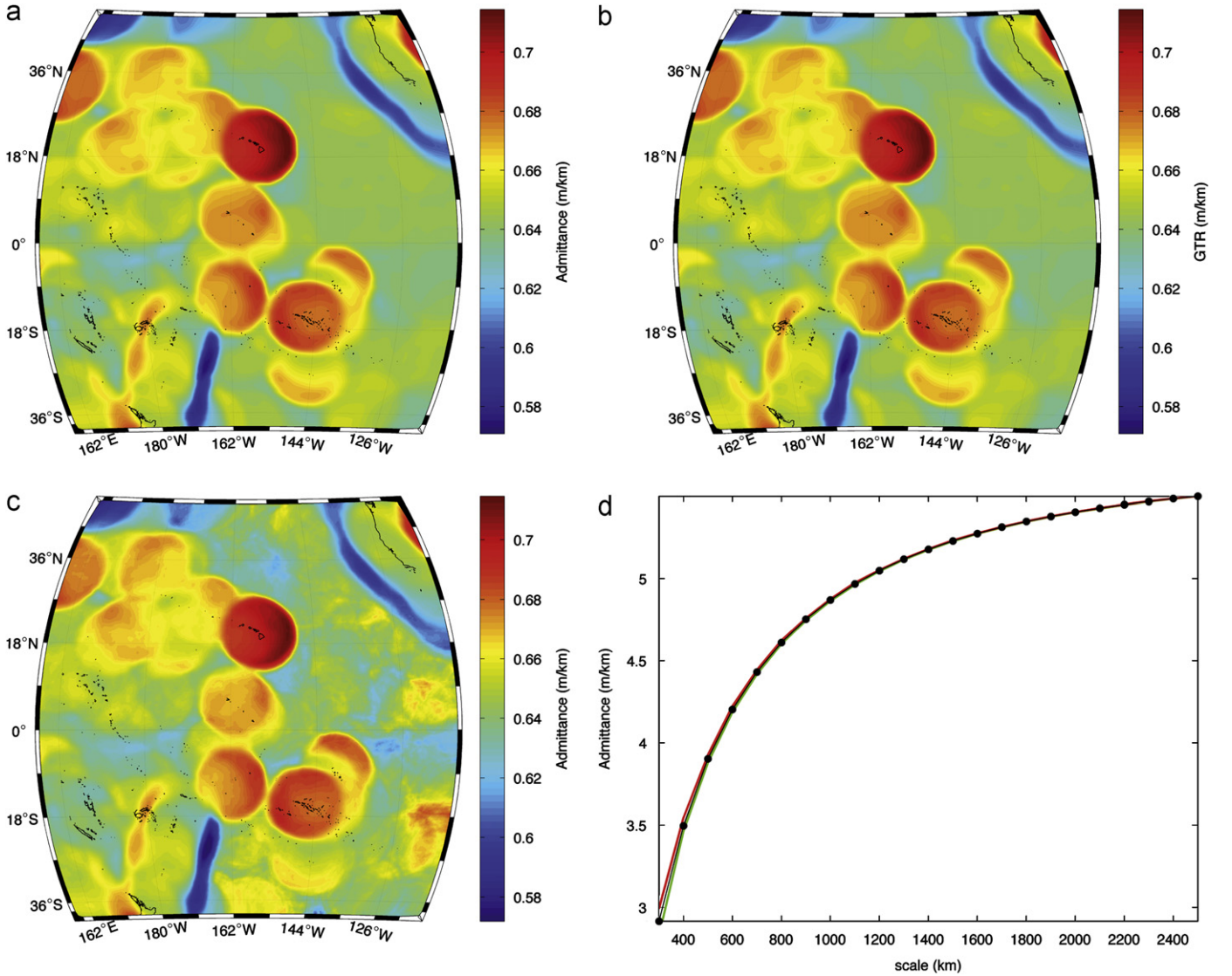
Fig. 3. Admittance using synthetic geoid data. Validation tests in the spatial domain: (a) the wavelet admittance from geoid anomalies using real topography, and assuming Airy compensation (Haxby and Turcotte, 1978), and the equivalent theoretical GTR (b) at 400 km scale. (c) The wavelet admittance from the noised synthetic geoid. Validation test in the spectral domain (d): the wavelet admittance (black curve) from geoid anomalies using real topography, and following Sandwell and Renkin (1988), and the theoretical admittance (black dots) represented at scales varying from 300 to 2500 km. Minimal and maximal admittance values from the noised synthetic geoid are shown by green and red curves respectively. (For interpretation of the references to color in this figure legend, the reader is referred to the web version of this article.)

a trade-off must be found to select the width factor s. The width of the averaging window sa must be superior to the correlation length of the CWT coefficients for each scale, but if sa is too large, the desired spatial localization is lost: when s goes to infinity, the global wavelet power spectrum is obtained. In this study, we use a Gaussian window function of the form $\Phi(x) = \exp\left(-x^2/2(sa)^2\right)$ with $s=2$ (Stark et al., 2003). Accordingly, the local wavelet auto-power spectra of the topography signal may be written as:

$$P_{h,h}^{\psi}(a,x) = \int C_h(a,e)C_h(a,e)\Phi_{sa}(x-e)de. \tag{5}$$

The obtained admittance function is interpretable only when the geoid and topography are sufficiently coherent. Thus, we define a coherence function that corresponds to the spatial correlation between the geoid and the topography, and hence indicates to what extent the admittance is meaningful (e.g. Kogan et al., 1985). Here, we interpret the admittance only if the associated coherence is superior to 0.5, a rather arbitrary threshold that is however higher than the ones generally considered in admittance studies

(for instance Kogan et al. (1985) used 0.2). In the next section, we show that the wavelet coherence can be affected by the measurement noise. Consequently, the geoid and the topography signals may be fully consistent despite a coherence around 0.5. The wavelet coherence C^{ψ} at scale a and position x is given by (Stark et al., 2003):

$$C^{\psi}(a,x) = \frac{P_{N,h}^{\psi}(a,x)^2}{P_{N,N}^{\psi}(a,x)P_{h,h}^{\psi}(a,x)} \tag{6}$$

with $P_{N,h}^{\psi}$ as the local wavelet auto-power spectra of the geoid signal. The coherence function varies between 0 (i.e., the two signals are uncorrelated) and 1 (i.e., the two signals are perfectly correlated).

3. Validation of the wavelet method

In order to establish the power of our wavelet method, we perform a series of tests. First, we validate the method using
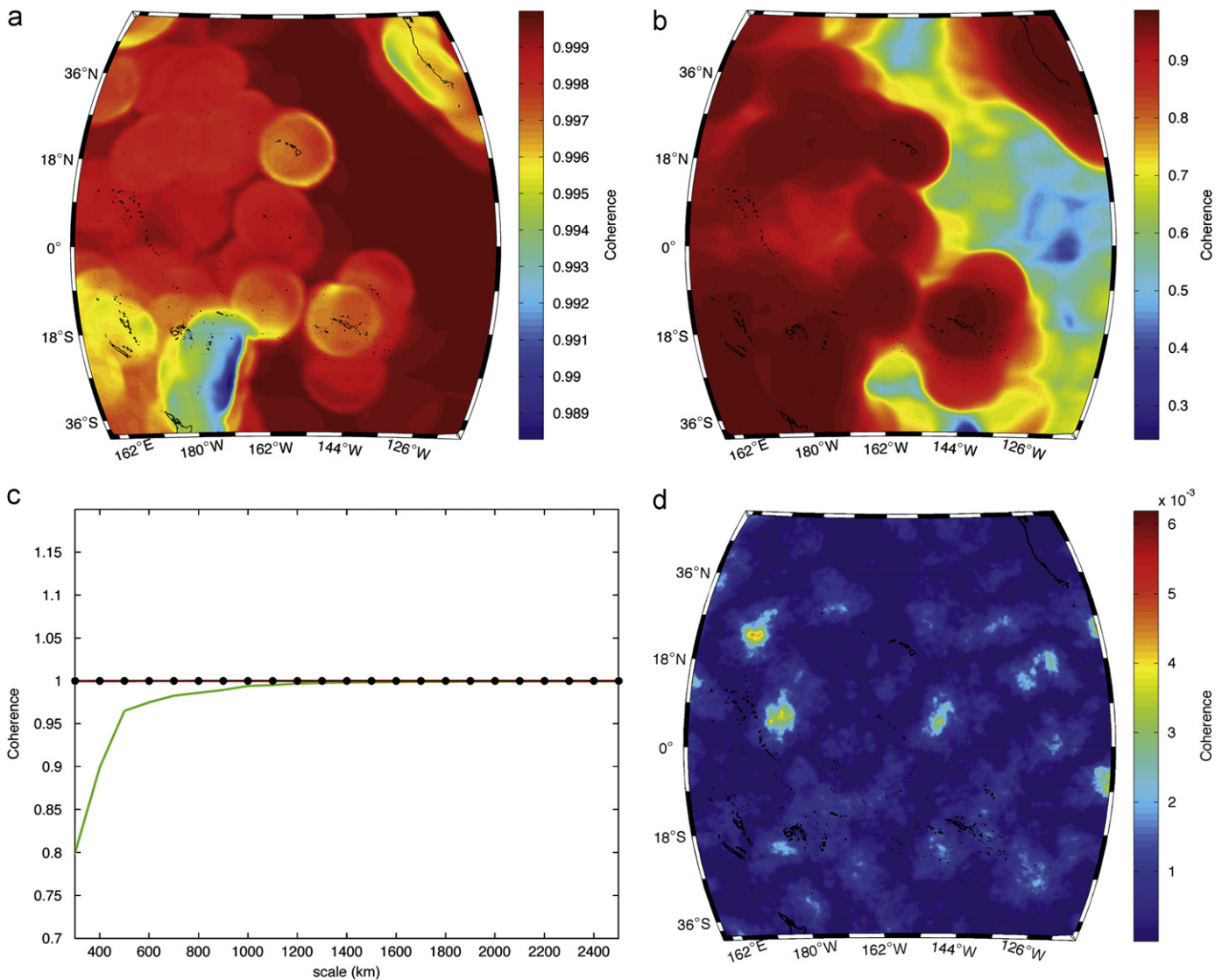
Fig. 4. Coherence using synthetic geoid data. Validation tests in the spatial domain: (a) the wavelet coherence from geoid anomalies using real topography, and assuming Airy compensation (Haxby and Turcotte, 1978) at 400 km scale. (b) The wavelet coherence from the noised synthetic geoid. Validation test in the spectral domain: (c) the wavelet coherence (black curve) from geoid anomalies using real topography, and following Sandwell and Renkin (1988), and the theoretical coherence (black dots) represented at scales varying from 300 to 2500 km. Minimal and maximal coherence values from the noised synthetic geoid are shown by green and red curves respectively. (d) The wavelet coherence from uncorrelated synthetic geoid and topography data at scale 400 km. (For interpretation of the references to color in this figure legend, the reader is referred to the web version of this article.)

synthetic data with well-known relationships between topography and geoid both in the spatial and the spectral domains. Then, we assess the wavelet admittance and coherence for synthetic data based on two geodynamic plume models (Ribe and Christensen, 1999; Ballmer et al., 2011), for which the characteristic swell formation mechanisms are known. Both these models match the height and the width of the Hawaiian swell, as well as the volume flux of Hawaiian shield stage volcanism (Ribe and Christensen, 1999; Ballmer et al., 2011). The geoid was not used as a constraint. The tests are illustrated in Figs. 3–7 and discussed below.

3.1. Validation tests in the spatial domain

In a first experiment, we test the ability of the wavelet method to recover known admittance values in each point at a given scale. At each scale, the synthetic geoid anomalies are generated from the real topography using the theoretical relationship given by Haxby and Turcotte (1978) for Airy compensation. The theoretical

admittance is then estimated in each point following Marks and Sandwell (1991) method (described above in the introduction) over sliding windows similar to the ones used in the wavelet approach. The wavelet admittance values and the equivalent theoretical admittance are mapped in the Fig. 3a and b respectively (here, we only show the results at 400 km scale as an example). The theoretical admittance is fully recovered by the wavelet method. Also, the wavelet coherence is very close to 1.0, confirming the expected perfect correlation between the geoid and the topography (Fig. 4a).

In a second experiment, a white noise was generated randomly and added to this geoid signal. The amplitude of imposed noise ranges from −20 to 20 cm at each scale. Although the noise biases the admittance only weakly (Fig. 3c), it reduces the coherence (Fig. 4b) because the geoid power spectrum is in the denominator of its expression (Eq. (6)). Nevertheless, only regions with relatively flat seafloor (i.e. with a low signal-to-noise ratio) are affected. Since the signal in our study area is huge, and the real measurement error is significantly smaller than the noise
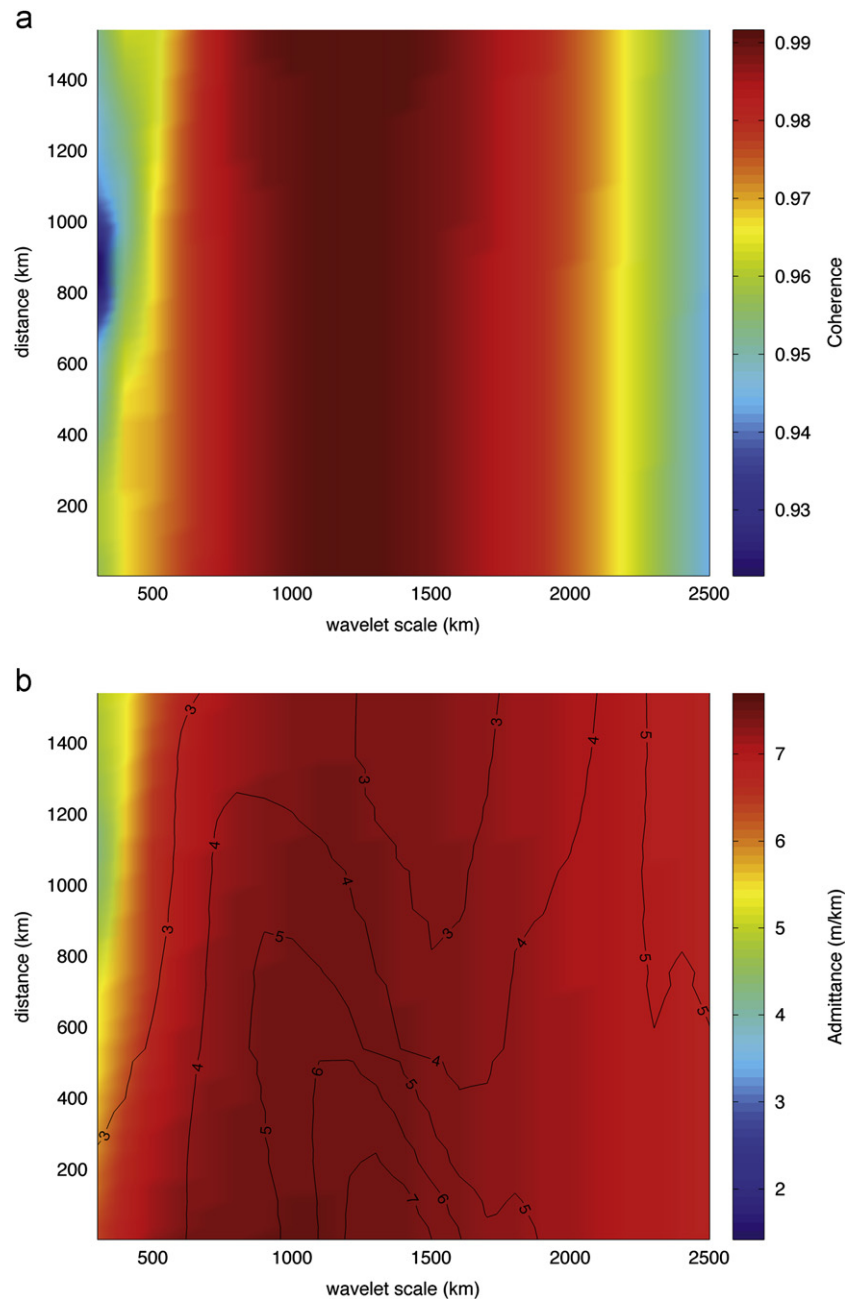
a

b

Fig. 5. Local wavelet coherence (top) and local wavelet admittance (bottom) derived from the Hawaiian plume model without volcanic loading (first geodynamic test), along the chain (y-axis) and at each analyzing scale (x-axis). The current hotspot location corresponds to zero on the y-axis. The wavelet scale varies between 100 and 2500 km. Contours denote the admittance as estimated from the data (see Fig. 10) for comparison.

imposed in this test in the wavebands that interest us (<1 cm at 400 km scale; see Section 4.1), we are confident that our method is reliable.

3.2. Validation tests in the spectral domain

In a third experiment, we evaluate the reliability of the wavelet admittance and coherence at each scale. We compare the wavelet admittance with the analytical solution given by Sandwell and Renkin (1988) for subsurface loading of an elastic lithosphere by thermal buoyancy forces. In that aim, a synthetic geoid is produced in the spectral domain from the real topography following Sandwell and Renkin (1988). The wavelet admittance agrees very well with the theoretical admittance at all scales (Fig. 3d), and the wavelet coherence persists at 1.0 (Fig. 4c).

In a fourth experiment, we add noise of the same amplitude as in the experiment 2 to the synthetic geoid. The minimal and maximal values of the corresponding wavelet admittance are represented in Fig. 3d. Noise in the geoid does not introduce bias into the estimates of the admittance at scales larger than 1300 km. However, at smaller scales the admittance values are very slightly affected by the noise. The same is true for the coherence (Fig. 4c), but with a higher decrease (see above). This bias is directly related to the size of the averaging widow, which is proportional to the wavelet scale, and thus smaller at these scales. Consequently, the variability introduced by the noise affects to a great degree the estimated admittance and coherence.

In a fifth and independent test, we consider the case for which no defined relationship between the topography and the geoid exists. Two synthetic datasets were created from random white
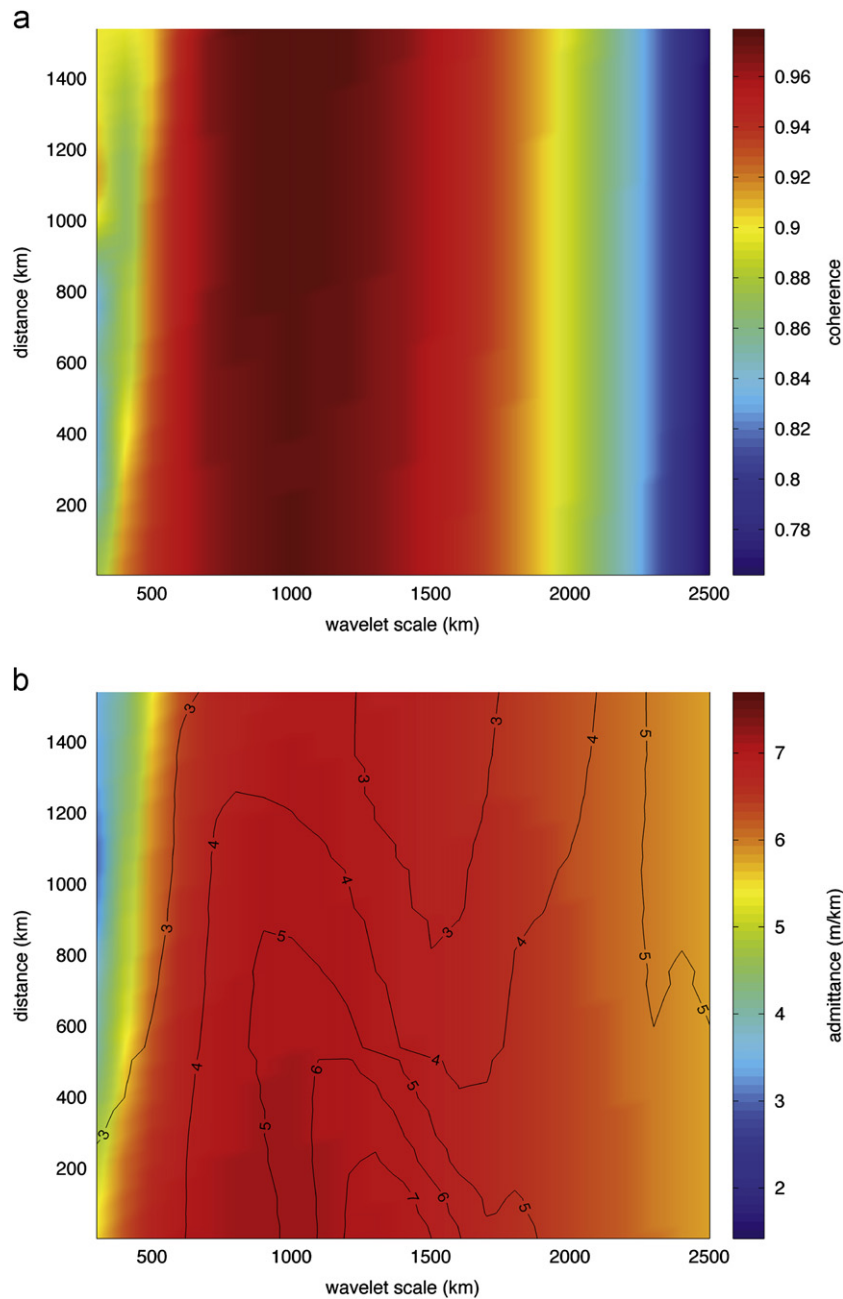
Fig. 6. Same as Fig. 5, but for the second geodynamic test including the effects of volcanic loading with $F=0.1$.

noise of the same amplitude as the geoid and the topography data. Fig. 4d shows that, as expected, the resulting wavelet coherence is very low at each point (<0.01).

3.3. Geodynamic test 1: synthetic plume

In a first geodynamic test, we compute the wavelet admittance using the synthetic topography and geoid as derived from the three-dimensional numerical plume model from Ribe and Christensen (1999). In this model, the applied numerical method simulates the dynamics of a stationary plume beneath a drifting lithosphere. The rheology of the fluid depends on pressure and temperature. The numerical domain is a rectangular box 400 km deep, 2304 km long, and 1152 km wide. The plume emerges from a fixed temperature anomaly at the bottom boundary that is open to vertical flow. Stresses at the bottom boundary are parameterized such that they account for the finite viscosity of the non-discretized fluid beneath

400 km depth. Partial melting as occurring predominantly at the hotspot is taken into account explicitly. Melting reduces the density of the residual mantle thereby affecting the buoyancy force and the geoid.

The synthetic topography anomaly is obtained by equating the vertical normal stress at the surface (as imposed by the convective flow beneath) to the sum of the isostatic weight of the lithospheric topography and the bending stresses in a thin elastic plate with flexural rigidity $D=1.7 \times 10^{23}$ Nm (Wessel, 1993). This calculation is dynamically self-consistent as long as the amplitude of the surface topography is much less than the depth of model box, in which limit of the convecting fluid "feels" the elastic lithosphere as an effectively rigid boundary moving at constant speed. The dynamic normal stress in the fluid is then independent of the lithosphere's flexural rigidity, which merely modifies the surface topography produced by that stress. Moreover, because the dynamic and flexural contributions to the topography are
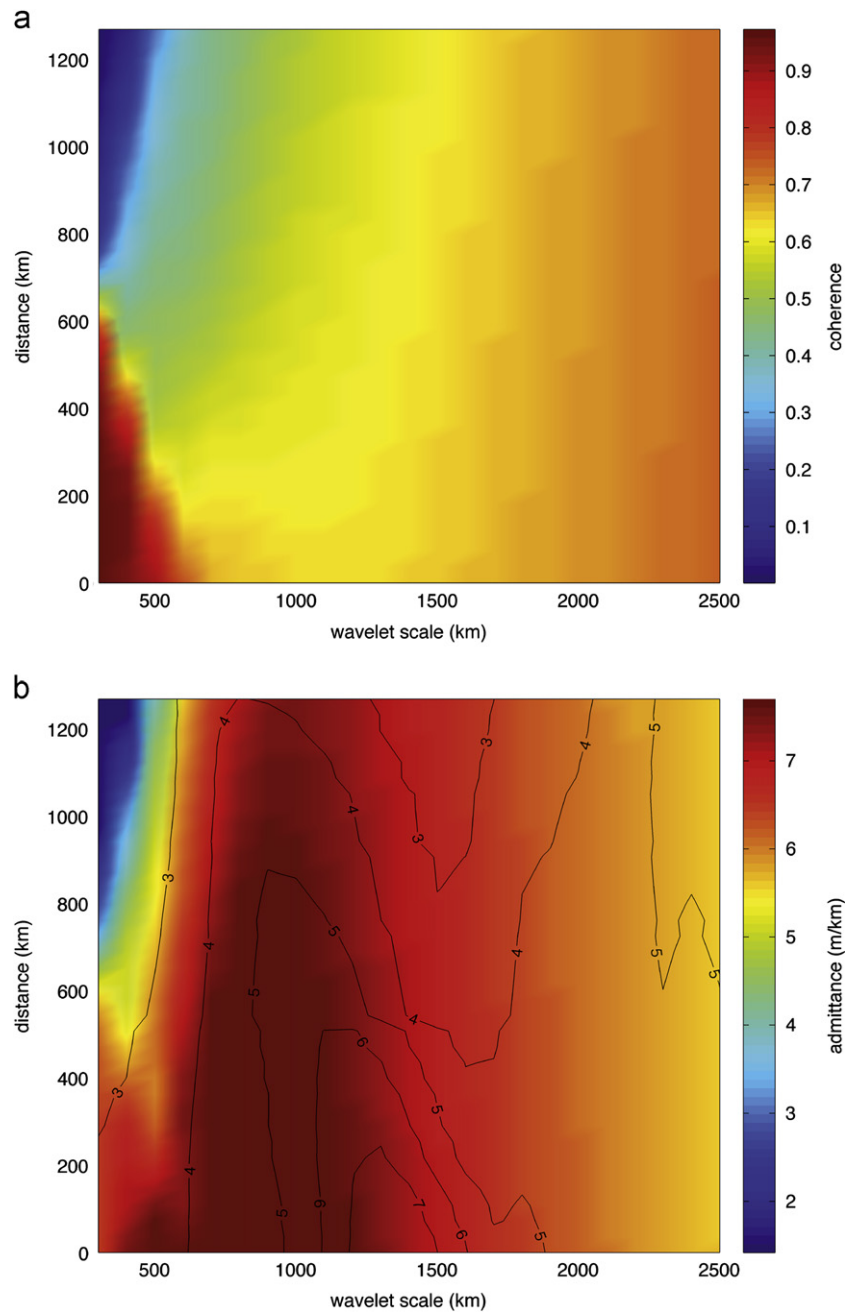
Fig. 7. Same as Fig. 5, but for the third geodynamic test including the effects of small-scale convection in the plume pancake.

separated without ambiguity in our (forward) models, our approach is not subject to the danger (pointed out by McKenzie, 2010) of using a flexural model to interpret topography with a dynamical origin. Once the topography has been determined, the geoid anomaly is calculated by summing the gravitational effects of the internal density distribution and the lithospheric topography. These computations and the model setup are described and discussed in detail by Ribe and Christensen (1999).

This specific test illustrates the signature of a plume in the wavelet coherence and admittance. The resulting coherence is superior to 0.9 on the whole chain and for all spatial scales (Fig. 5a). The admittance peaks at ∼7.5 m/km in the 1000–1500 km scale band, which is consistent with the characteristic scales of the synthetic swell topography and geoid (Ribe and Christensen, 1999; Cserepes et al., 2000). As the coherence peaks in a very similar range of scales, we are confident that these predictions are reliable. The admittance

values of 7–7.5 m/km derived from this test indeed reproduce the average geoid-to-topography ratio of 7–8 m/km estimated by Ribe and Christensen (1999) and Cserepes et al. (2000), which both apply the well-established Marks and Sandwell (1991) method.

3.4. Geodynamic test 2: synthetic plume with volcanic surface loading

In addition to the effects of an upwelling plume treated above, we consider those of volcanic loading in a second test. It is assumed that the melt migrates vertically to the surface to build volcanic edifices equivalent to the Hawaiian island chain. These edifices (separated by an interval of 252 km) modify surface topography and geoid both by its mere presence, and by bending the lithosphere elastically (Cserepes et al., 2000). Since estimating the total volume of the melt emplaced on top of the plate is

subject to big uncertainties (cf. van Ark and Lin, 2004; Vidal and Bonneville, 2004; Robinson and Eakins, 2006), we consider four different scenarios. We assume that only a given melt fraction F of any magmas predicted from the geodynamic model to be generated in the mantle actually erupts at the surface. In order to constrain F, we compare the synthetic and observed geoid and topography for various F ($F=0.0$, 0.1, 0.5 and 1.0). Fig. S1 shows that $F=0.1$ yields the best agreement between model predictions and observations.

We evaluate the effects of volcanic loading with $F=0.1$ on both the wavelet coherence and admittance. The resulting coherence is high at the characteristic scales of the Hawaiian swell and at scales smaller than 400 km, which are most sensitive to the presence of the volcanic islands (Fig. 6a). The admittance peaks at 7.1 m/km (Fig. 6b), is similar to the maximum in the first test (7.5 m/km). In comparison with the first test, we note only a slight decrease of the local admittance values at large scales. At scales inferior to ∼400 km, however, this decrease is significant with the minimum admittance dropping to 3 m/km (as opposed to 4.3 m/km for the first geodynamic test).

This synthetic test establishes that the wavelet admittance method indeed allows isolation of the signals related to volcanic loading and lithospheric flexure. While these effects strongly influence the small scales of our wavelet analysis, we are able to recover admittance values of 7–7.5 m/km in the characteristic scale band of the swell. In contrast, the Marks and Sandwell (1991) method yields a GTR value of only ∼4 m/km for the whole swell (Cserepes et al., 2000). We note however that models with a fraction of erupted melt $F > 0.1$ also display admittances < 7 m/km in the scale band of the swell. This is because larger F implies more voluminous islands with smaller distances between them. The geoid anomalies associated with these volcanic edifices then overlap each other, so that even at the large scales the wavelet approach cannot completely separate the contribution of volcanic loading from that of the swell.

3.5. Geodynamic test 3: synthetic plume with small-scale convection in the pancake

In a third test, we apply the wavelet method on the synthetic topography and geoid derived from a three-dimensional numerical model that simulates the interaction of small-scale sublithospheric convection (SSC) with a mantle plume (Ballmer et al., 2011). In many ways, the geodynamic model used for this third test (Ballmer et al., 2011) is similar to that used in the tests above (Ribe and Christensen, 1999). However, the model setup differs in some crucial details that allow for development of SSC within the plume pancake. Most importantly, these differences concern the rheology of the mantle: a higher Rayleigh-number and activation energy yield a significantly lower viscosity in the hottest part of the plume compared to the Ribe and Christensen (1999) model. Therefore, vigorous SSC develops within the hot center of the plume pancake on the downstream side of the hotspot (i.e. beneath the Hawaiian Islands). Due to the choice of the rheology (i.e., Newtonian rheology with high activation energy) and the initial flatness of the incoming lithosphere, the vigor of SSC remains a conservative prediction (cf. van Hunen et al., 2003; Huang et al., 2003). Accordingly, the vigor of SSC as developing within the flanks of the pancake is underestimated. Additional differences to the Ribe and Christensen (1999) models involve the depth of the box (660 km) and the bottom boundary condition (closed to vertical flow well away from the plume center). Such a treatment of the bottom boundary assumes partial layering of the mantle. The full description of the model is given in the supplementary material of Ballmer et al. (2011) with the specific case described in section SB and Fig. S3.

The synthetic geoid and topography in this third test are derived in a manner analogous to the tests above; they are derived from the gravitational effects of the density distribution within the model domain and the vertical stresses at the surface, respectively. The effect of lithospheric topography on the geoid is also explicitly included. In contrast to the tests above, not only the effect of depletion of the residue by partial melting on mantle density, but also that of retention of a small melt fraction (up to 1%) is considered. However, our results are insensitive to this assumption.

The wavelet coherence of the third test reflects the characteristics of SSC in the plume pancake. Although at scales > 600 km, the coherence is generally higher than our reference value of 0.5, it is systematically lower than in the first two tests (Fig. 7a). At scales < 600 km, the coherence peaks close to the hotspot (> 0.9), but very rapidly decreases down the chain (< 0.5). Although upwelling and downwelling limbs of SSC should produce coherent signals by simultaneously producing topography and geoid undulations at the surface, they also redistribute masses at the base of the lithosphere on a broad range of scales (Fig. S2). Such a redistribution affects the topography and the geoid, but in a different manner, reducing the coherence. For example, sublithospheric erosion occurring in a narrow channel along the central axis of the plume pancake accounts for the systematic decrease of the coherence at scales < 600 km. Along these lines, we are confident to interpret wavelet admittances at the scale band of the swell, where coherences are moderately high.

The admittance reveals two maxima at the current hotspot location: one at scales of ∼500 km, and another one at scales of ∼800 km (Fig. 7b). Futhermore, it decreases systematically along the chain at scales 300–600 km: the GTR varies from 8 m/km on the island of Hawaii (i.e., the hotspot) to 6 m/km on Kauai. This decrease indicates a decay of the average depth of compensation by ∼20 km (cf. Haxby and Turcotte, 1978). This rate of decay is consistent with the regional effects of small-scale convection to erode the base of the lithosphere by 15–20 km along a narrow channel in the center of the plume pancake (Ballmer et al., 2011; Fig. S2). In the 600–1200 km scale range, the admittance also decays along the chain, but only very slowly (i.e. from 8 m/km close to the hotspot to 7.6 m/km near Kauai). Such a decay indicates a decrease of the average depth of compensation by only 4 km, reflecting the weakness of lithospheric erosion induced by SSC on the flanks of the plume pancake in the geodynamic model.

This final synthetic test illustrates the power of our wavelet method to resolve spatial variations of the wavelet admittance. Thus, we can clearly distinguish between two physical contributions to swell support: dynamic support by the ponding plume and lithospheric thinning induced by SSC.

3.6. Test conclusion

The series of validation and geodynamic tests show that the wavelet approach is robust and well suited to estimate the local characteristics of the coherence and admittance along the Hawaiian chain at different spatial scales. Therefore, we are able to constrain the variation of the average depth of the low-density material that compensates the swell from the data. Moreover, by comparison with the geodynamic tests, wavelet analysis of the data potentially allows identification of the underlying physical mechanisms of swell formation. For example, we expect that dynamic support by the ascending plume generates a GTR on the order of 7–8 m/km in the characteristic scale band of the swell. Also, we establish above that SSC within the plume pancake gradually reduces the GTR along the chain. Finally, volcanic

loading and the associated lithospheric flexure are expected to significantly reduce the admittance, an effect that is however limited to scales smaller than 500 km. This latter prediction is in agreement with Cserepes et al. (2000) and shows that it is essential to completely remove the influence of the volcanic load in order to avoid the risk of underestimating the compensation depth of the swell.

4. Application to the Hawaiian swell

4.1. Geoid and topography data

In this study, we analyze high-resolution geoid data from the GRACE mission measurements (Tapley et al., 2004). This mission provides geoid models of unprecedented precision at wavelengths larger than 200 km, which have hence been used to study e.g. the South Pacific Superswell (Panet et al., 2006; Cadio et al., 2011). Here, for the first time, we apply this data to study the Hawaiian swell. Specifically, we use geoid anomalies derived from the global spherical harmonics model EIGEN-GL04C (Förste et al., 2008) up to degree and order 360. The precision on the geoid is about 2–3 mm at 400 km resolution. Accordingly, the geoid is accurately mapped in the characteristic waveband of the swell.

The bathymetric grid used in this study is extracted from the global compilation from GEBCO (General Bathymetric Chart of the Oceans). It is exclusively derived from echosounder measurements and hence does not rely on a dataset that is biased by predictions from gravity anomalies (i.e., satellite altimetry). The resolution of the bathymetric grid is 1 min.

We carry out our wavelet analysis with and without correcting for the effects of seafloor age. Thermal cooling of the aging oceanic lithosphere affects both seafloor depth and geoid height: seafloor depth increases and geoid height decreases with seafloor age. Any corrections are made according to the seafloor depth-to-age relationship from the GDH1 plate model (Stein and Stein, 1992), and to the geoid-height to seafloor-age relationship from Turcotte and Schubert (2002). Seafloor ages are taken from Müller et al. (2008). Our main results are insensitive to whether or not we perform these corrections (see Fig. S3 in supplemental materials). Therefore, and considering the uncertainties of the above relationships in the vicinity of hotspots, in what follows, we only discuss the results obtained without the correction for seafloor age.

4.2. Wavelets analysis

We apply a continuous wavelet transform (CWT) to the geoid and topography anomalies measured in the vicinity of the Hawaiian hotspot at scales ranging from 100 to 2500 km (Figs. 8 and 9). Wavelets are specifically suited to study this area, which is characterized by a superimposition of structures on a broad range of scales.

Each scale is sensitive to a distinct geological feature. At scales inferior to 500 km, the signature of volcanic edifices and the flexural arch dominates the signals. We also note two maxima near the intersections between the seamount chain and the Murray and Molokai fracture zones, respectively. These observations concur with Wessel (1993), and suggest that the Hawaiian plume may interact in some way or another with sublithospheric topography along the fracture zones (Epp, 1984; McNutt et al., 1989; Yamamoto and Phipps Morgan, 2009). At intermediate scales (500–1700 km), the geoid and topography anomalies reflect the signature of the swell as a whole. These signatures are best expressed between the two fracture zones with the amplitude of the geoid and topography anomalies generally decreasing towards the northwest. However, this decrease is not exactly monotonic. The swell appears as two quasi-elliptic regions centered on Molokai (202.5°E, 21.5°N) and the Gardner Pinnacles (192°E, 24.5°N), a constellation that has been interpreted as the result of past variations in the magmatic activity of the Hawaiian hotspot (e.g. Davies, 1992; Van Ark and Lin, 2004; Vidal and Bonneville, 2004). For scales of ∼1700 km and greater, the geoid and topography anomalies are not associated with the Hawaiian swell. For example, the topography anomaly as located west of the Hawaiian chain is related to the Mid-Pacific Seamounts. Furthermore, the apparent geoid anomaly south of the Hawaiian archipelago likely reflects the Hawaiian plume stem, an interpretation that is in good agreement with a recent regional body-wave tomography (Wolfe et al., 2009).

4.3. Wavelet admittance and coherence

Fig. 10 shows the local wavelet admittance and coherence along the Hawaiian chain, at each scale, as calculated from the CWT coefficients. On the youngest part of the chain, the coherence is higher than 0.5 throughout the scale band of interest, and higher than 0.7 for scales < 1000 km. With increasing distance from the hotspot center, it gradually yet slowly decreases. Consequently, the observed data are robust for interpretation at the spectral and spatial scales of interest.

Since the data are processed analogously to the synthetic tests above, we can directly compare the observed admittances to the predicted ones. At scales smaller than 500 km, the admittance does not exceed 4 m/km and is similar to that obtained at the same scales in the second synthetic test (cf. Section 3.4). The signature of volcanic loading thus dominates the admittance patterns. Consequently, it masks any other contributions in this range of scales, such as that of SSC, which is characterized by a higher admittance and a lower coherence. Indeed, the second synthetic test shows that the presence of volcanic loading considerably reduces the admittance and leads to an increase of the coherence at scales for which SSC occurs. The superposition of volcanic loading and SSC can thus explain the discrepancy between the observations and the hybrid model at these scales. At scales greater than 800 km, the admittance sharply increases to ∼8 m/km at scales between 1100 and 1600 km. Such an admittance indicates sublithospheric compensation, and according to the first synthetic test (cf. Section 3.3), is fully in accord with dynamic support by a mantle plume. Indeed, the corresponding scales are consistent with the characteristic dimensions of the Hawaiian swell.

However, these high admittance values are only retrieved very close to the current hotspot location and do not represent the greatest part of the Hawaiian chain. With increasing distance from the hotspot, the admittance decreases from 8 m/km close to the hotspot to 6 m/km near Kauai. This decrease indicates that the compensation depth of the swell gradually decreases by 20 km over a distance of ∼500 km to the northwest. The scale of this decrease corresponds to the scale of the swell, and its rate is similar to the predictions of the third synthetic test, which involves sublithospheric erosion by SSC beneath the swell (cf. Section 3.5). However, in the specific geodynamic model used for the third test, SSC occurs at spatial scales that are smaller than those of the swell, and hence cannot fully explain the observed scale range of the decay of the admittance. Only a subtle decrease of the admittance is predicted at these scales in the third test. This discrepancy indicates that SSC beneath the flanks of the Hawaiian swell is more vigorous than predicted by the third geodynamic test.
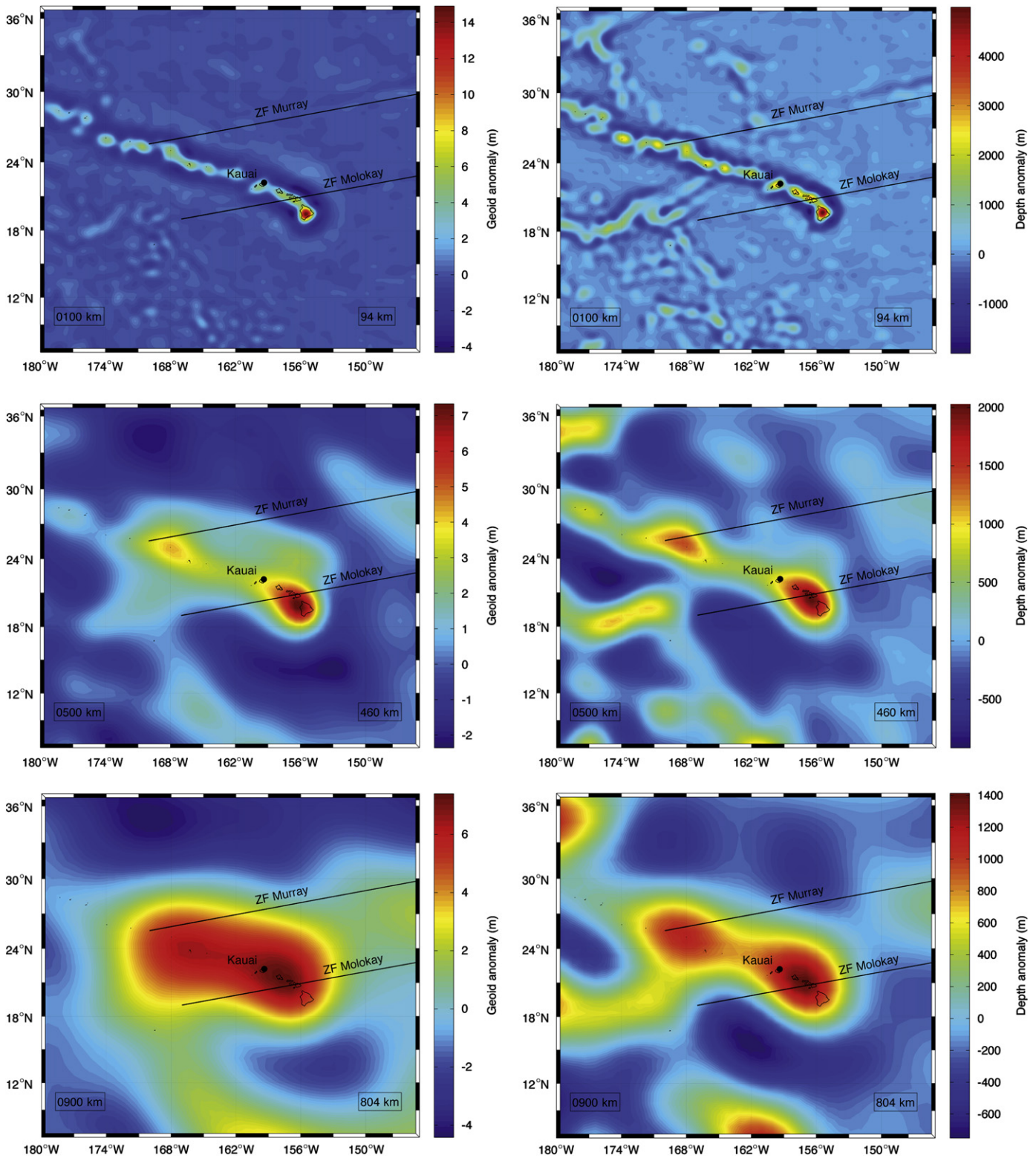
Fig. 8. Continuous wavelet analysis of the EIGEN-GL04C geoid model (on the left) and the GEBCO topography (on the right) on the Hawaiian swell at scales of 100, 500 and 900 km (from top to bottom). The analyzing wavelet scale and the corresponding maximal depth of compensating density anomalies for the GTR are given on the bottom left and on the bottom right of each panel, respectively.

5. Discussion

We show that the wavelet approach allows proper quantification of the GTR of the Hawaiian swell at its characteristic scales. With ~8 m/km on the youngest part of the chain, this novel approach yields a significantly higher GTR than previous studies, which are all limited in terms of jointly resolving the spatial and spectral characteristics of the signals (Crough, 1978; McNutt and Shure, 1986; Cazenave et al., 1988; Sandwell and Renkin, 1988; Sandwell and MacKenzie, 1989; Marks and Sandwell, 1991). This achievement emerges from the ability of the applied wavelet to completely eliminate the unwanted contribution from volcanic
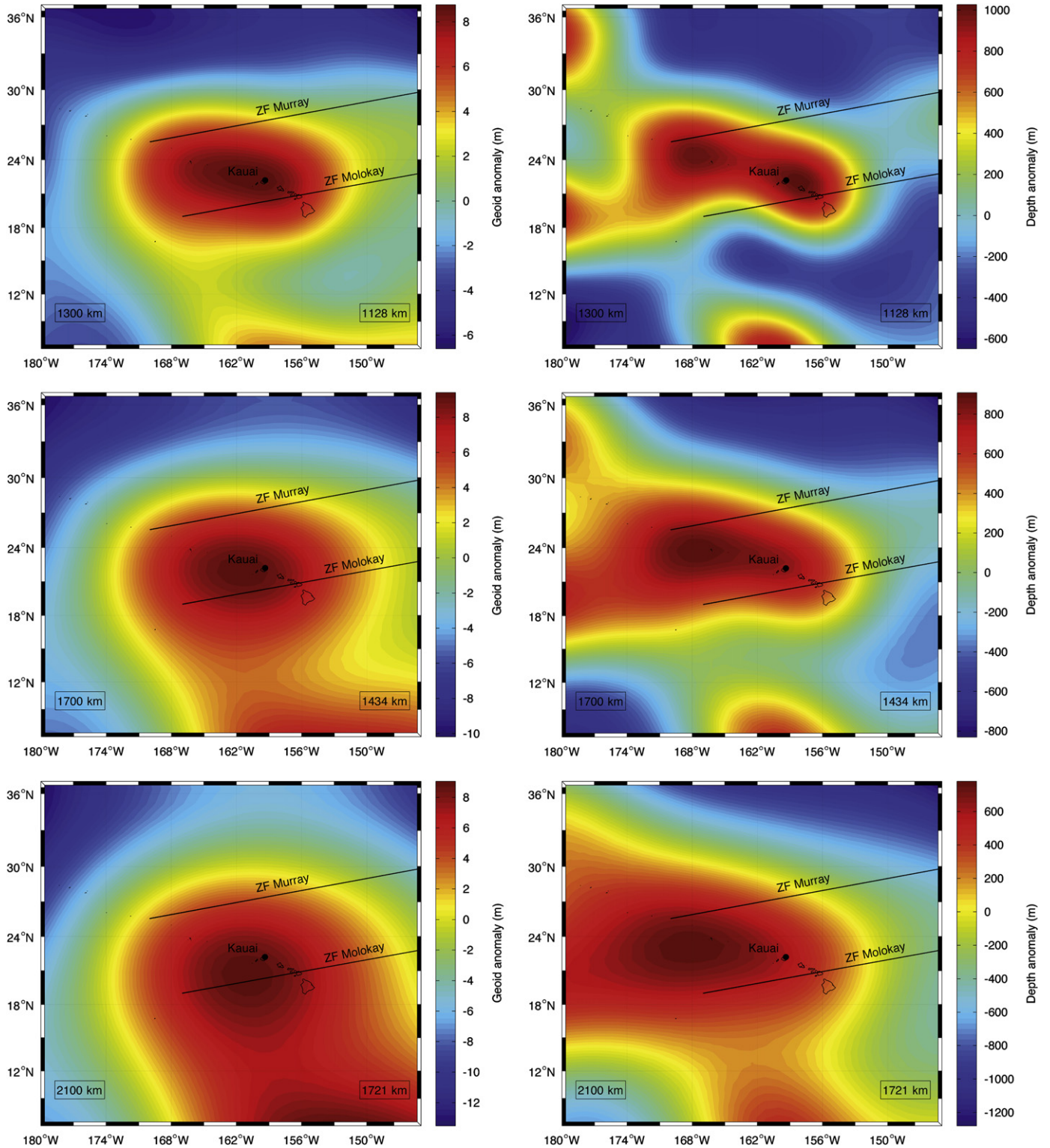
Fig. 9. Continuous wavelet analysis of the EIGEN-GL04C geoid model (on the left) and the GEBCO topography (on the right) on the Hawaiian swell at scales of 1300, 1700 and 2100 km (from top to bottom). The analyzing wavelet scale and the corresponding maximal depth of compensating density anomalies for the GTR are given on the bottom left and on the bottom right of each panel, respectively.

loading, an effect that would otherwise act to reduce the GTR by almost a factor of two. Therefore, our method yields for the first time satisfactory agreement between the observed GTR and the synthetic GTR as derived from plume models.

Accordingly, our analysis can provide important constraints on the compensation mechanism of the Hawaiian swell. It not

only rules out the thermal rejuvenation model (Crough, 1978), but also agrees well with the predictions of the dynamic support model. In the framework of mantle plume theory, the swell would be dynamically supported by ponding of a deep-rooted mantle plume beneath the lithosphere (Morgan, 1972; Sleep, 1990; Ribe and Christensen, 1994, 1999). Recent seismic
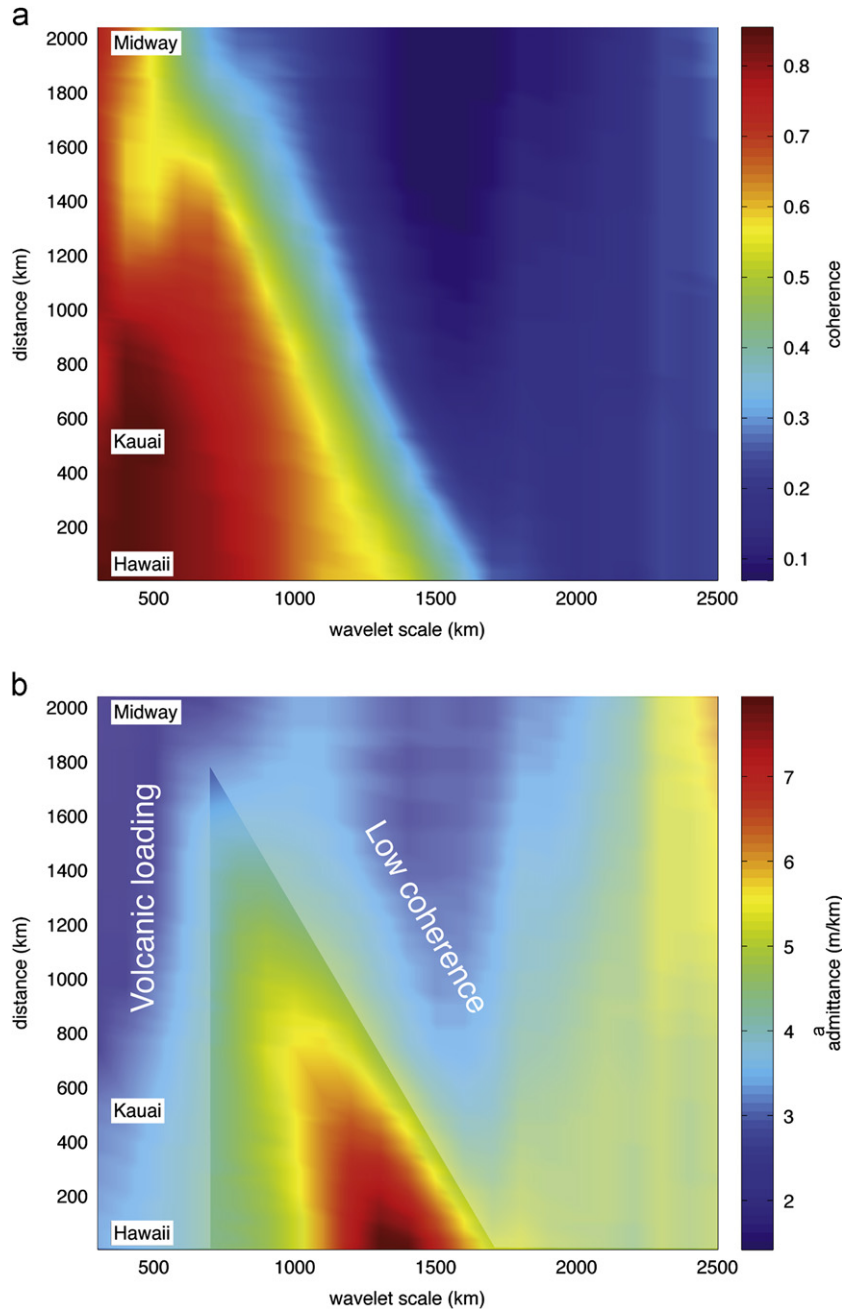
Fig. 10. Local wavelet coherence (top) and local wavelet admittance (bottom) along the chain and at each analyzing scale, as based on the data (cf. Figs. 8 and 9). The current hotspot location corresponds to zero on the vertical axis.

tomography lends further credibility to this concept (Wolfe et al., 2009).

However, controversy persists as to whether Hawaiian volcanism is in fact sustained by a mantle plume (Anderson, 2010), GTR analysis alone is an inadequate tool to settle this debate. In the case of Hawaii, constraining the depth of origin of the plume from the admittance pattern is difficult for at least two reasons. First, the signal associated with the lateral density contrasts between the plume conduit and the rest of the mantle is swamped by the presence of the islands and the flexural moat. Second, the plume stem is inferred to be located not directly beneath the swell, but rather displaced southward (cf. Wolfe et al., 2009). Thus, any deflection of the upper–lower mantle boundary affecting the geoid (e.g. Hager, 1984) cannot directly contribute to the admittance pattern. In spite of these shortcomings, the good match

between synthetic admittance patterns and observations is a strong case for a deep origin of Hawaiian volcanism.

Furthermore, we are able to quantify the decay of the GTR along the chain in the characteristic scale band of the swell. Applying the wavelet method to the plume model with SSC in its pancake, we recover a rate of decay that is very similar to the observed one. However, the numerical model predicts this decay to be most apparent at scales smaller than about 700 km. Such an admittance pattern cannot be recovered in the data since these scales are strongly influenced by volcanic loading and lithospheric flexure (this study; Cserepes et al., 2000). Hence, the apparent decay of the GTR in the characteristic range of scales of the swell remains to be fully explained.

Nevertheless, we believe that more realistic configurations of SSC in the pancake can account for the decay of the GTR at these

scales (Ribe, 2004). In the specific geodynamic model tested (cf. Section 3.5), SSC occurs most vigorously in the central parts of the pancake (i.e., beneath the islands), and much less at its flanks (Ballmer et al., 2011). This is the configuration which causes lithospheric erosion to be limited to a narrow scale band (Fig. S2). However, we have not yet explored several of the parameters that strongly influence the dynamics of the pancake, such as reference viscosity, activation energy, plume excess temperature, and plume radius. Two of these four parameters can be varied independently for given dimensions of the swell (Ribe and Christensen, 1994). More specifically, the considered model (cf. Section 3.5) accurately accounts for the effects of diffusion creep in the mantle with a realistic activation energy for this mechanism (i.e., 300 kJ/mol, cf. Karato and Wu, 1993), but neglects those of dislocation creep. While diffusion creep is indeed expected to be the most important deformation mechanism in the hot plume core, dislocation creep has been shown to be dominant at the edges of the plume, where stresses are greatest (Asaadi et al., 2011). Therefore, we expect a lower viscosity, as well as more vigorous SSC and lithospheric erosion along the flanks of the pancake than predicted by our model (cf. van Hunen et al., 2003). Furthermore, pre-existing heterogeneity at the base of the lithosphere, which is also not included in our model, would be expected to further enhance SSC (Huang et al., 2003; Ballmer et al., 2011). Along these lines, we believe that in a somewhat more realistic model, SSC may be able to explain the gradual decrease of the GTR on scales up to ∼1000 km, and hence to satisfy the constraints from our wavelet analysis.

This expectation is supported by seismic observations that indicate sublithospheric erosion along the Hawaiian swell (Li et al., 2004; Schmerr, 2012). Using underside reflections, Schmerr (2012) shows that the Pacific lithosphere thins by ∼10 km along the Hawaiian chain over lateral scales of ∼1000 km. Using receiver functions, Li et al. (2004) suggest much greater thinning of ∼50 km. Although it is not obvious that Li et al. (2004) actually image the base of the lithosphere, we think that the combined seismic evidence is a strong support for our interpretation of sublithospheric erosion at the characteristic scales of the swell.

Other mechanisms may contribute to support the swell, but can hardly offer a good explanation for the full characteristics of the GTR. For example, Leahy et al. (2010) find seismic evidence for crustal underplating around the islands, and hence suggest that the swell is compensated in large part by a shallow chemical anomaly. However, the high admittance values that we recover suggest a much deeper average depth of compensation. Also, Leahy et al. (2010) find that the thickness of the underplated layer is approximately constant below the whole swell, and hence cannot provide an explanation for the gradual decay of the GTR.

An alternative explanation for the apparent decrease in the compensation depth of the swell may include lithospheric thickness variations across fracture zones. Such a model has already been proposed for the Marquesas and Line Islands (cf. Epp, 1984; McNutt et al., 1989). While the step in lithospheric thickness across the Molokai Fracture Zone (FZ) may indeed contribute to the gradual decrease of the GTR towards the northwest, the expected increase of the GTR near the Murray FZ is not seen by our analysis. Nevertheless, our coherence estimates gradually decrease from the Molokai FZ towards the Murray FZ, thus we cannot make any clear conclusion in this area from our analysis.

We show in this manuscript that the wavelet analysis of the geoid and topography, and the related benchmark with synthetic tests based on geodynamic models can constrain the compensation mechanisms of hotspot swells. For the Hawaiian swell application, the effects of SSC on the flanks of the plume pancake, or of fracture zones remain to be quantified in such a synthetic tests. Also, the effects of plume buoyancy flux variations (Davies,

1992; Vidal and Bonneville, 2004) on spatial variations of the GTR remain to be tested.

6. Conclusion

In order to elucidate the dominant mechanisms of Hawaiian swell support, we apply a continuous wavelet transform of the geoid and topography. The estimation of the wavelet admittance allows accurate mapping of the geoid to topography ratio along the swell, and thus of its average compensation depth. Comparison of the observed wavelet admittance with those predicted from several synthetic tests shows that our approach can remove the unwanted contributions from volcanic loading, and distinguish between at least two important compensation mechanisms. These include dynamic support by a mantle plume, and lithospheric thinning such as e.g. induced by small-scale convection.

In our analysis, we find that the Hawaiian swell is mainly supported dynamically by a mantle plume. However, an additional mechanism is required to account for the slow decay of the admittance along the Hawaiian chain. One of our synthetic tests including small-scale convection in the center of the plume pancake is indeed able to recover the rate of this decay, but not its full spectral characteristics. Nevertheless, in accord with seismic evidence for lithospheric thinning along the Hawaiian chain (e.g., Schmerr, 2012), we propose that additional small-scale convection on the flanks of the pancake can resolve this discrepancy. While more advanced studies are needed to test this hypothesis, we establish that our wavelet approach – including the comparison with synthetic tests – is a powerful tool to quantify the styles of mantle convection that support hotspot swells, and feed intraplate volcanism.

Appendix A. Supporting information

Supplementary data associated with this article can be found in the online version at http://dx.doi.org/10.1016/j.epsl.2012.10.006.

References

Abouchami, W., Hofmann, A.W., Galer, J.G., Frey, F.A., Eisele, J., Feigenson, M., 2005. Lead isotopes reveal bilateral asymmetry and vertical continuity in the Hawaiian mantle plume. Nature 434, 851–856.

Anderson, D.L., 2010. Hawaii, boundary layers and ambient mantle – geophysical constraints. J. Petrol. , http://dx.doi.org/10.1093/petrology/egq068.

Asaadi, N., Ribe, N.M., Sobouti, F., 2011. Inferring nonlinear mantle rheology from the shape of the Hawaiian swell. Nature, 473, http://dx.doi.org/10.1038/nature09993.

Audet, P., 2011. Directional wavelet analysis on the sphere: application to gravity and topography of the terrestrial planets. J. Geophys. Res. 116, E01003, http://dx.doi.org/10.1029/2010JE003710.

Ballmer, M.D., Ito, G., van Hunen, J., Tackley, P.J., 2011. Spatial and temporal variability in Hawaiian hotspot volcanism induced by small-scale convection. Nat. Geosci., 4, http://dx.doi.org/10.1038/ngeo1187.

Cadio, C., Panet, I., Davaille, A., Diament, M., Métivier, L., de Viron, O., 2011. Pacific geoid anomalies revisited in light of thermochemical oscillating domes in the lower mantle. Earth Planet. Sci. Lett., 306, http://dx.doi.org/10.1016/j.epsl.2011.03.040.

Cazenave, A., Dominh, K., Rabinowicz, M., Ceuleneer, G., 1988. Geoid and depth anomalies over ocean swells and troughs: evidence of an increasing trend of the geoid to depth ratio with age of plate. J. Geophys. Res. 93, 8064–8077.

Ceuleneer, G., Rabinowicz, M., Monnereau, M., Cazenave, A., Rosemberg, C., 1988. Viscosity and thickness of the sub-lithospheric low viscosity zone: constraints from geoid and depth over oceanic swells. Earth Planet. Sci. Lett. 89, 84–102.

Chambodut, A., Panet, I., Mandea, M., Diament, M., Holschneider, M., Jamet, O., 2005. Wavelet frames: an alternative to spherical harmonic representation of potential fields. Geophys. J. Int. 163 (3), 875–899, http://dx.doi.org/10.1111/j.1365-246X.2005.02754.x.

Crosby, A.G., McKenzie, D., 2009. An analysis of young ocean depth, gravity and global residual topography. Geophys. J. Int. 178 (3), 1198–1219.

Crough, S.T., 1983. Hotspot swells. Ann. Rev. Earth Planet. Sci 11, 165–193.

Crough, S.T., 1978. Thermal origin of mid-plate hot-spot swells. Geophys. J. R. Astron. Soc. 55, 451–469.

Cserepes, L., Christensen, U.R., Ribe, N.M., 2000. Geoid height versus topography for a plume model of the Hawaiian swell. Earth Planet. Sci. Lett. 178, 29–38.

Daly, E., Brown, C., Stark, C.P., Ebinger, C.J., 2004. Wavelet and multitaper coherence methods for assessing the elastic thickness of the Irish Atlantic margin. Geophys. J. Int. 159 (2), http://dx.doi.org/10.1111/j.1365-246X.2004.02427.x.

Davies, G.F., 1992. Temporal variation of the Hawaiian plume flux. Earth Planet. Sci. Lett. 113, 277–286.

Detrick, R.S., Crough, S.T., 1978. Island subsidence, hot spots, and lithospheric thinning. J. Geophys. Res. 83, 1236–1244.

Dietz, R.S., Menard, H.W., 1953. Hawaiian swell, deep, and arch, and subsidence of the Hawaiian Islands. J. Geol. 61, 99–113.

Epp, D., 1984. Possible perturbations to hotspot traces and implications for the origin and structure of the Line Islands. J. Geophys. Res. 89, 11273–11286.

Förste, C., Schmidt, R., Stubenvoll, R., Flechtner, F., Meyer, U., König, R., Neumayer, H., Biancale, R., Lemoine, J., Bruinsma, S., Loyer, S., Franz, B., Esselborn, S., 2008. The GeoForschungsZentrum Potsdam/Groupe de Recherche de Géodésie Spatiale satellite-only and combined gravity field models: EIGEN-GL04S1 and EIGEN-GL04C. J. Geod., 82, http://dx.doi.org/10.1007/s00190-007-0183-8.

Garcia, M.O., Swinnard, L., Weis, D., Greene, A.R., Tagami, T., Sano, H., Gandy, C.E., 2010. Petrology, Geochemistry and Geochronology of kaua'i Lavas over 4 center dot 5 Myr: implications for the origin of rejuvenated volcanism and the evolution of the Hawaiian plume. J. Petrol. 51, 1507–1540.

Hager, B.H., 1984. Subducted slabs and the geoid: constraints on mantle rheology and flow. J. Geophys. Res. 89, 6003–6015.

Harris, R.N., Von Herzen, R.P., McNutt, M.K., Garven, G., Jordahl, K., 2000. Submarine hydrogeology of the Hawaiian archipelagic apron 1. Heat flow patterns north of Oahu and Maro reef. J. Geophys. Res. 105 (B9), 21353–21369.

Haxby, W., Turcotte, D., 1978. On isostatic geoid anomalies. J. Geophys. Res. 83 (B11), 5473–5478.

Holschneider, M., 1995. Wavelets: An Analysis Tool. Oxford Sciences Publications, Oxford.

Holschneider, M., Chambodut, A., Mandea, M., 2003. From global to regional analysis of the magnetic field on the sphere using wavelet frames. Phys. Earth Planet. Inter. 135, 107–124.

Huang, J.S., Zhong, S.J., van Hunen, J., 2003. Controls on sublithospheric small-scale convection. J. Geophys. Res. 108 (B8), 2405.

Karato, S.-I., Wu, P., 1993. Rheology of the upper mantle: a synthesis. Science 260, 771–778, http://dx.doi.org/10.1126/science.260.5109.771.

Kirby, J.F., Swain, C.J., 2004. Global and local isostatic coherence from the wavelet transform. Geophys. Res. Lett. 31 (24), L24608, http://dx.doi.org/10.1029/2004GL021569.

Kogan, M.G., Diament, M., Bulot, A., Balmino, G., 1985. Thermal isostasy in the South Atlantic Ocean from geoid anomalies. Earth Planet. Sci. Lett. 74, 280–290.

Leahy, G.M., Collins, J.A., Wolfe, C.J., Laske, G., Solomon, S.C., 2010. Underplating of the Hawaiian swell: evidence from teleseismic receiver functions. Geophys. J. Int. 183, 313–329.

Li, X., Kind, R., Yuan, X., Wölbern, I., Hanka, W., 2004. Rejuvenation of the lithosphere by the Hawaiian plume. Nature 427, 827–829.

Marks, K., Sandwell, D.T., 1991. Analysis of geoid height versus topography for oceanic plateaus and swells using non-biased linear regression. J. Geophys. Res. 96, 8045–8055.

McKenzie, D., 2010. The influence of dynamically supported topography on estimates of Te. Earth Planet. Sci. Lett. 295, 127–138, http://dx.doi.org/10.1016/j.epsl.2010.03.033.

McKenzie, D., Bowin, C., 1976. The relationship between bayhymetry and gravity in the Atlantic ocean. J. Geophys. Res. 31 (11), 1903–1915.

McNutt, M.K., 1984. Lithospheric flexure and thermal anomalies. J. Geophys. Res. 89 (B13), 11180–11194.

McNutt, M.K., Shure, L., 1986. Estimating the compensation depth of the Hawaiian swell with linear filters. J. Geophys. Res. 91, 13915–13923.

McNutt, M., Fischer, K., Kruse, S., Natland, J., 1989. The origin of Marquesas fracture zone ridge and its implications for the nature of hotspots. Earth Planet. Sci. Lett. 91, 381–393.

Moore, W., Schubert, G., Tackley, P., 1998. Three-dimensional simulations of plume lithosphere interaction at the Hawaiian swell. Science 279, 1008–1011.

Moore, W., Schubert, G., Tackley, P., 1999. The role of rheology in lithospheric thinning by mantle plumes. Geophys. Res. Lett. 26 (8), 1073–1076.

Morgan, W.J., 1972. Deep mantle convection plumes and plate motions. Bull. Am. Assoc. Petrol. Geol. 56, 203–213.

Müller, R.D., Sdrolias, M., Gaina, C., Roest, W.R., 2008. Age, spreading rates, and spreading asymmetry of the world's ocean crust. Geochem. Geophys. Geosyst. 9, Q04006, http://dx.doi.org/10.1029/2007GC001743.

Olson, P., 1990. Hot spots, swells and mantle plumes. in: Ryan, M.P. (Ed.), Magma Transport and Storage. John Wiley, New York, pp. 33–51.

Panet, I., Mikhailo, V., Diament, M., Pollitz, F., King, G., de Viron, O., Holschneider, M., Biancale, R., Lemoine, J.M., 2007. Co-seismic and post-seismic signatures of the Sumatra December 2004 and March 2005 earthquakes in GRACE satellite gravity. Geophys. J. Int., 171, http://dx.doi.org/10.1111/j.1365-246X.2007.03525.x.

Panet, I., Chambodut, A., Diament, M., Holschneider, M., Jamet, O., 2006. New insights on intraplate volcanism in French Polynesia from wavelet analysis of GRACE, CHAMP, and sea surface data. J. Geophys. Res. 111, B09403, http://dx.doi.org/10.1029/2005JB004141.

Parsons, B., Daly, S., 1983. The relationship between surface topography, gravity anomalies and temperature structure of convection. J. Geophys. Res. 88, 1129–1144.

Parsons, B., Sclater, J.G., 1977. An analysis of the variation of ocean floor bathymetry and heat flow with age. J. Geophys. Res. 82, 802–827.

Ribe, N.M., 2004. Through thick and thin. Nature 427, 793–795.

Ribe, N.M., Christensen, U.R., 1999. The dynamical origin of Hawaiian volcanism. Earth Planet. Sci. Lett. 171, 517–531.

Ribe, N.M., Christensen, U.R., 1994. Three-dimensional modeling of plume–lithosphere interaction. J. Geophys. Res. 99 (B1), 669–682.

Robinson, J.E., Eakins, B.W., 2006. Calculated volumes of individual shield volcanoes at the young end of the Hawaiian Ridge. J. Volcanol. Geotherm. Res. 151, 309–317.

Robinson, E.M., Parsons, B., 1988. Effect of a shallow low-viscosity zone on the formation of midplate swells. J. Geophys. Res. 93, 3144–3156.

Robinson, E.M., Parsons, B., Daly, S.F., 1987. The effect of a shallow low viscosity zone on the apparent compensation of mid-plate swells. Earth Planet. Sci. Lett. 82, 335–348.

Sandwell, D.T., MacKenzie, K.R., 1989. Geoid height versus topography for oceanic plateaus and swells. J. Geophys. Res. 94, 7403–7418.

Sandwell, D.T., Renkin, M.L., 1988. Compensation of swells and plateaus in the North Pacific: no direct evidence for mantle convection. J. Geophys. Res. 93, 2775–2783.

Schmerr, N., 2012. The Gutenberg discontinuity: melt at the Lithosphere–Asthenosphere boundary. Science 335, 1480–1483.

Sleep, N.H., 1994. Lithospheric thinning by midplate mantle plumes and the thermal history of hot plume material ponded at sublithospheric depths. J. Geophys. Res 99, 9327–9343.

Sleep, N.H., 1990. Hotspots and mantle plumes: some phenomenology. J. Geophys. Res. 95, 6715–6736.

Stark, C., Stewart, J., Ebinger, C., 2003. Wavelet transform mapping of effective elastic thickness and plate loading: validation using synthetic data and application to the study of southern African tectonics. J. Geophys. Res. 108 (B12), 2558, http://dx.doi.org/10.1029/2001JB000609.

Stein, C.A., Stein, S., 1992. A model for the global variation in oceanic depth and heat flow with age. Nature 359, 123–129.

Tapley, B.D., Bettadpur, S., Watkins, M., Reigber, C., 2004. The gravity recovery and climate experiment: mission overview and early results. Geophys. Res. Lett. 31, L09607, http://dx.doi.org/10.1029/2004GL019920.

Turcotte, D., Schubert, G., 2002. Geodynamics, 2nd ed. Cambridge University Press, Cambridge.

Van Ark, E., Lin, J., 2004. Time variation in igneous volume flux of the Hawaii-Emperor hot spot seamount chain. J. Geophys. Res. 109, B11401, http://dx.doi.org/10.1029/2003JB002949.

Vidal, V., Bonneville, A., 2004. Variations of the Hawaiian hot spot activity revealed by variations in the magma production rate. J. Geophys. Res. 109, B03104, http://dx.doi.org/10.1029/2003JB002559.

Von Herzen, R.P., Cordery, M.J., Detrick, R.S., Fang, C., 1989. Heat flow and the thermal origin of hot spot swells: the Hawaiian swell revisited. J. Geophys. Res. 94 (B10), 13783–13799.

Yuen, D., Fleitout, L., 1985. Thinning of the lithosphere by small-scale convective destabilization. Nature 313, 125–128.

van Hunen, J., Huang, J.S., Zhong, S.J., 2003. The effect of shearing on the onset and vigor of small-scale convection in a Newtonian rheology. Geophys. Res. Lett. 30 (19), 1991.

Wessel, P., 1993. Observational constraints on models of the Hawaiian hot spot swell. J. Geophys. Res. 98 (B9), 16095–16104.

Wolfe, C.J., Solomon, S.C., Laske, G., Collins, J.A., Detrick, R.S., Orcutt, J.A., Bercovici, D., Hauri, E.H., 2009. Mantle shear-wave velocity structure beneath the Hawaiian hotspot. Science 326, 1388–1390.

Yamamoto, M., Phipps Morgan, J., 2009. North Arch volcanic fields near Hawaii are evidence favouring the restite-root hypothesis for the origin of hotspot swells. Terra Nova 21 (6), 452–466.